Journal of Alloys and Compounds 928 (2022) 167177

Contents lists available at ScienceDirect

Journal of Alloys and Compounds

journal homepage: www.elsevier.com/locate/jalcom

Elucidation of formation and transformation mechanisms of Ca-rich Laves phase in Mg-Al-Ca-Mn alloys

Jiehua Li[a,b,*], Xuyang Zhou[a], Andrew Breen[a], Zirong Peng[a], Jing Su[a], Philipp Kürnsteiner[a], Maria Jazmin Duarte Correa[a], Marta Lipińska Chwałek[c,d], Huiyuan Wang[e], David Holec[f], Joachim Mayer[c,d], Gerhard Dehm[a]

[a] Max-Planck Institut für Eisenforschung, Max-Planck-Strasse 1, D-40237 Düsseldorf, Germany
[b] Institute of Casting Research, Montanuniversität Leoben, A-8700 Leoben, Austria
[c] Central Facility for Electron Microscopy, RWTH Aachen University, 52074 Aachen, Germany
[d] Ernst Ruska-Centre (ER-C) for Microscopy and Spectroscopy with Electrons, Forschungszentrum Jülich GmbH, 52425 Jülich, Germany
[e] Key Laboratory of Automobile Materials of Ministry of Education, School of Materials Science and Engineering & International Center of Future Science, Jilin University, No. 5988 Renmin Street, Changchun 130025, PR China
[f] Department of Materials Science, Montanuniversität Leoben, A-8700 Leoben, Austria

ARTICLE INFO

Article history:
Received 10 July 2022
Received in revised form 7 August 2022
Accepted 12 September 2022
Available online 15 September 2022

Keywords:
Mg alloy
Laves phase
Phase transformation
DFT simulation
Transmission electron microscopy
Atom probe tomography

ABSTRACT

The formation of thermally stable intermetallic phases plays a key role to enable high temperature applications for Mg alloys. In the ductile Mg-Al-Ca system, Ca-rich Laves phases are expected to be crucial for improving high temperature mechanical properties. However, the formation mechanisms of Ca-rich Laves phases are still unresolved. Here, we report atomic-scale experiments and simulations on transformation of Ca-rich Laves phases and formation of Ca-rich clusters as well as Ca-segregation behaviour in Mg-Al-Ca-Mn alloys in three conditions: as-cast, homogenised (500 °C, 20 h), and rolled (350 °C). The formation mechanisms of C36 Laves phase and Mg-rich particles (eutectic Mg) within C36 Laves phase were attributed to a divorced eutectic reaction. The transformation mechanisms from C36 to C15 Laves phase were revealed and discussed in terms of Mg out-diffusion of C36 Laves phase, the partitioning of Al into C36 Laves phase and the change of stacking sequences. The combined atomic-scale experimental and simulation investigation reveals complex interactions among various Ca-rich Laves phases in Mg-Al-Ca-Mn alloys.

1. Introduction

Mg alloys, as the lightest structural metallic materials, benefit from several property combinations such as high specific strength with respect to weight, good strength at room temperature as well as relatively large thermal and electrical conductivities [1]. However, its application potential is still very limited compared to steel and Al due to some disadvantages such as a relatively complicated processing environment requiring gas protection for melting, casting and deformation, and poor corrosion properties necessitating a surface treatment. Among its various disadvantages, at least two important disadvantages greatly hamper its wider application. Firstly, the mechanical properties of conventional Mg-Al based alloys (i.e. AZ91, AM60) at elevated temperatures (i.e. up to 120 °C) are not adequate due to the presence of $Mg_{17}Al_{12}$ phase. Being one of the most important strengthening phases for low temperature applications, $Mg_{17}Al_{12}$ phase can provide effective strengthening effects of conventional Mg-Al based alloys only up to 120 °C due to the softening of $Mg_{17}Al_{12}$ phase and thereby the loss of its strengthening effect [2]. How to reduce or avoid the formation of $Mg_{17}Al_{12}$ phase is a key point for the further development of Mg-Al based alloys. Ca alloying of Mg-Al based alloys was reported not only to suppress formation of $Mg_{17}Al_{12}$ phase but, at the same time, to promote formation of various high melting temperature Ca-rich Laves phases [3–13], which can greatly improve the strength of the alloy at temperatures exceeding 120 °C. Three different Ca-rich Laves phases have been reported to form in Mg-Al-Ca based alloys: $(Mg,Al)_2Ca$ C36 Laves phase (hexagonal, hP24, Ni_2Mg prototype, space group P63/mmc, #194), Al_2Ca C15 Laves phase (cubic, cF24, Cu_2Mg prototype, space group Fd-3m, #227) and Mg_2Ca C14 Laves phase (hexagonal, hP12, Zn_2Mg prototype, space group P63/mmc, #194) [14–27]. Although the structure, composition and transformation of these Ca-rich Laves phases has been widely investigated by

* Corresponding author at: Institute of Casting Research, Montanuniversität Leoben, A-8700 Leoben, Austria.
E-mail address: jiehua.li@unileoben.ac.at (J. Li).

https://doi.org/10.1016/j.jallcom.2022.167177

modelling and experiments [14–27], a detailed atomic-scale experimental and simulation study of the formation and transformation mechanisms of Ca-rich Laves phases is still lacking. Their formation and transformation mechanisms of Ca-rich Laves phases are of central importance to control and optimise the performance of Mg-Al-Ca based alloys.

Prior to the formation of Ca-rich Laves phases along grain boundaries, solute segregation of Al and Ca to grain boundaries may take place in Mg-Al-Ca based alloy, which can improve the formability of Mg-Al-Ca based alloy. In fact, improving the formability of Mg alloys is also one of the major challenges to advance applications of Mg alloys. Since Mg possesses a hexagonal close-packed (hcp) structure, it has less slip systems available for plastic deformation than cubic alloys (e.g. Al or steel) [1]. Micro-alloying with Ca can be employed to weaken the texture via solute segregation and deformation induced segregation to grain boundaries and thereby improve the formability of Mg alloys [5]. For example, in binary Mg-Ca alloys, the addition of a small amount of Ca (0.47 wt%) improved the ductility of Mg alloys through enhancing the activity of non-basal < a+c > slip [5]. Still, the physical and thermodynamic mechanisms of solute segregation and the deformation-induced segregation to grain boundaries in Mg-Al-Ca based alloys remain unexplored. In fact, the physical and thermodynamic mechanisms of solute segregation in Mg-Al-Ca based alloys is far from being fully understood, particularly because of all the synergy effects resulting from the different alloying elements and their misfits as solutes in the Mg matrix.

Accordingly, our study focuses on these two unresolved topics. We investigate and discuss segregation of Ca solute and formation of Ca-rich clusters as well as the transformation of Ca-rich Laves phases in Mg-3Al-1Ca and Mg-3Al-1Ca-1Mn (wt%) alloys in three processing conditions: as-cast, homogenised (500 °C, 20 h), and rolled (350 °C). A particular focus is given to the partitioning of Al and the formation of Mg-rich particles within Ca-rich Laves phases and their effect on the transformation of Ca-rich Laves phases, elucidated with the aid of atom probe tomography (APT), high resolution transmission electron microscopy (TEM), and scanning transmission electron microscope (STEM) with high angle annular dark field (HAADF) imaging and energy-dispersive X-ray spectroscopy (EDS). Density functional theory (DFT) calculations were also employed to validate the TEM and APT observations. On the basis of this detailed atomic-scale experimental and simulation study, two possible concepts about how tailoring the Ca segregation along grain boundaries and controlling the formation of Ca-rich Laves phases are proposed for further improving the performance of Mg-Al-Ca based alloys.

2. Methods

2.1. Specimen preparation

Alloys with nominal compositions of Mg-3Al-1Ca and Mg-3Al-1Ca-1Mn (wt%, used through the paper unless stated otherwise) were prepared from high purity Mg (99.9 %), Al (99.9 %), Mg-10Ca and Mg-10Mn master alloys. The alloys were melted in an electric resistance furnace under protective-gas mixture (CO_2 with 1 vol % SF_6) and cast into a die mould at about 760 °C. Solution treatment was performed at 500 °C for 20 h and followed by quenching into cold water. A subsequent rolling was performed at 350 °C with a total thickness reduction of 78 % and a final thickness of 1 mm. The same experimental procedure was applied to both investigated Mg-3Al-1Ca and Mg-3Al-1Ca-1Mn alloys. A comparative investigation of Mg-3Al-1Ca and Mg-3Al-1Ca-1Mn alloys aims to clarify the effect of Mn-alloying on the segregation behaviour of Ca solute and subsequent formation of Ca-rich clusters as well as transformation of Ca-rich Laves phases (and/or Mn-rich intermetallic phases). For comparison, other Mg-Ca binary alloys and Mg-3Al-Ca ternary alloys were also prepared using the same procedure.

2.2. Microstructure characterisation

Scanning electron microscopy (SEM) and electron backscatter diffraction (EBSD) measurements were performed by using a Carl Zeiss Cross Beam 1540EsB equipped with an HKL EBSD detector with a step size of 0.2 µm (for as-cast, homogenised samples). EBSD data analysis was performed using the TSL software (TSL Version 8.0). The samples for EBSD were metallographically prepared using SiC papers and 50 nm diameter silica suspension (water-free), and subsequently argon ion beam milled for 1 h using Hitachi IM4000 system. TEM samples and APT specimens were prepared by an in-situ lift-out method [28,29] in a focused ion beam (FIB) instrument FEI Helios Dual Beam SEM/FIB 600/600i. Conventional TEM including selected area diffraction pattern (SADP) was performed using a Tecnai G2 F20 operated at 200 KV. HAADF STEM imaging and EDS analyses of TEM samples were conducted with the aid of a probe-corrected FEI Titan G2 80–200 operated at 200 KV or a probe-corrected Hitachi HF5000 operated at 200 KV. APT experiments were performed on a LEAP 3000X HR (CAMECA Instruments, Madison, WI, USA) local electrode atom probe with a voltage-pulsed mode or LEAP5096XR (CAMECA Instruments, Madison, WI, USA) local electrode atom probe with a voltage-pulsed mode. The pulse repetition rate was 200 kHz and the target detection rate reached 5 detection events per 1000 pulses. The pressure in the analysis chamber at the level of 3×10^{-11} Torr and the specimen base temperature of 50 K were maintained during measurements. APT data reconstruction and analysis were performed using Imago Visualisation and Analysis Software (AP Suite 6).

2.3. Mechanical properties

Tensile specimens with a gage length of 4 mm, gage width of 1.8 mm and thickness of 1 mm were machined from the as-rolled sheets along the rolling direction (RD) and tested by using a Kamrath & Weiss stage coupled with digital image correlation (DIC) technique at room temperature with an initial strain rate of 1.0×10^{-3} s^{-1}. At least two samples were tested for each condition. The reported values were taken from the average of tested values. Global and local strains were also measured by DIC.

2.4. DFT simulation

DFT calculations were performed with the aid of Vienna Ab initio Simulation Package (VASP) [30,31] and the projector-augmented wave pseudopotentials [32]. The quantum mechanical electron-electron interactions were treated on the level of generalised gradient approximation (GGA) as parametrised by Perdew, Burke and Ernzerhof [33]. The Monkhorst-Pack k-mesh [34] was Gamma-point centered with the k-points spacing of approximately 0.04 $Å^{-1}$. Default cut-off energies for the plane-wave expansion were assumed to be defined by the pseudopotentials, i.e. 270 eV for the combination of Ca_sv, Mg, Mn_pv and Al potentials. The electronic self-consistent cycles were considered converged when the total energy change was less than 10^{-6} eV per simulation box. Structural relaxations including changes of the unit cell shape, volume and atomic positions, were converged to the total energy change of 10^{-4} eV per cell. For the substitutional studies, only the atomic positions were relaxed. The energy of formation (E_f) was calculated as:

$$E_f = E_{tot}(\mathrm{supercell}) - \sum_i n_i \mu_i \quad (1)$$

where $E_{tot}(supercell)$ is the total energy of a supercell containing n_i atoms of species i with the chemical potential μ_i. These parameters

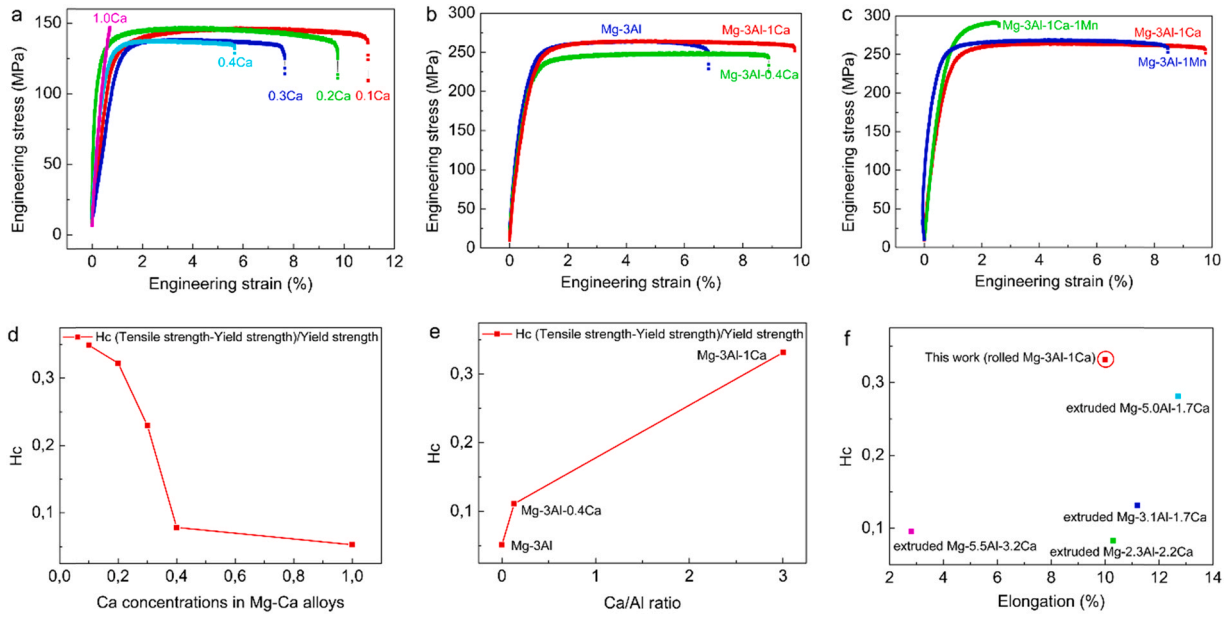

Fig. 1. Mechanical properties of Mg-xCa (x: 0.1, 0.2, 0.3, 0.4, 1.0) binary alloys, Mg-3Al-yCa (y: 0, 0.4, 1.0) ternary alloys and Mg-3Al-1Ca-1Mn alloy. (a, b, c) engineering stress vs engineering strain curves, (d, e) the strain hardening capacity (Hc (UTS-YS)/YS) as a function of Ca concentrations in Mg-Ca binary alloys and the Ca/Al ratio in Mg-3Al-Ca ternary alloys. (f) a comparison of the strain hardening capacity (Hc (UTS-YS)/YS) V.S. elongation in different deformed Mg-Al-Ca based alloys.

were set using fcc-Al, hcp-Mg, hex-Ca, and A12-Mn. VESTA3 software was used for visualising the structures [35].

3. Results

In this section, we firstly report mechanical properties and strain hardening capacity of Mg-Ca binary alloys and Mg-3Al-Ca ternary alloys as well as Mg-3Al-1Ca-1Mn quaternary alloy after rolling. Then, we report a detailed TEM and APT characterisation of Ca-rich Laves phases in Mg-3Al-1Ca ternary alloy and Mg-3Al-1Ca-1Mn quaternary alloy. Finally, we also report DFT simulation in order to further support our TEM and APT observations. We can clearly demonstrate a good agreement between TEM, APT observation and DFT simulation.

3.1. Mechanical properties and strain hardening capacity of Mg-Ca binary alloys and Mg-3Al-Ca ternary alloys as well as Mg-3Al-1Ca-1Mn alloy after rolling

In order to elucidate the effect of Ca concentrations on the mechanical properties in Mg-Ca binary alloy and Mg-3Al-Ca ternary alloy, five Mg-xCa binary alloys with different Ca concentrations (0.1, 0.2, 0.3, 0.4, 1.0) and three Mg-3Al-yCa (0, 0.4, 1.0) ternary alloys after rolling were investigated. Tensile testing of Mg-xCa binary alloys revealed that with increasing Ca concentrations in Mg-Ca binary alloys, ultimate tensile strength (UTS) and yield strength (YS) increases but the elongation decreases, as shown in Fig. 1a and Fig. S1a. In contrast, with increasing Ca concentrations in Mg-3Al-Ca ternary alloys, UTS decreases firstly and then increases slightly, YS decreases but the elongation increases, as shown in Fig. 1b and Fig. S1b. The addition of Mn (1 wt%) increases UTS and YS but decreases

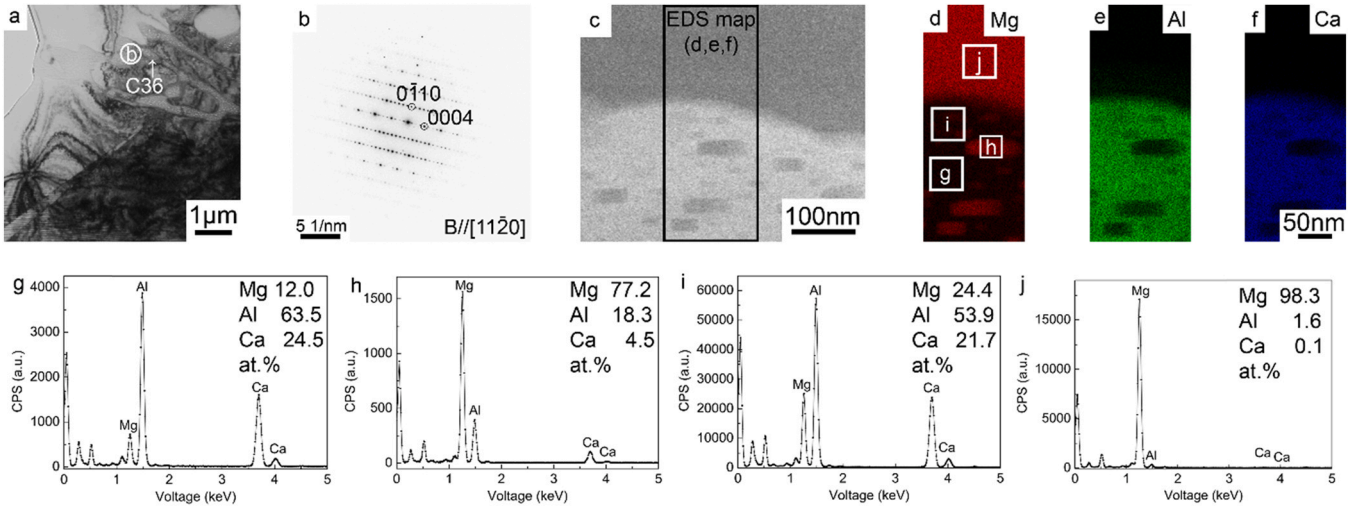

Fig. 2. TEM characterisation of the Ca-rich Laves phase of Mg-3Al-1Ca alloy in the as-cast condition. (a) bright field TEM image, (b) SADP of C36 Laves phase (as marked in (a)), (c) enlarged HAADF-STEM image of the same region as (a) and the selected regions for EDS analysis, (d-f) EDS maps of Mg, Al, Ca, (g–j) quantitative EDS analyses of the selected regions (pure C36 (g), Mg-rich particle (h), C36 together with Mg-rich particle (i), and pure Mg matrix (j)) as marked in (d).

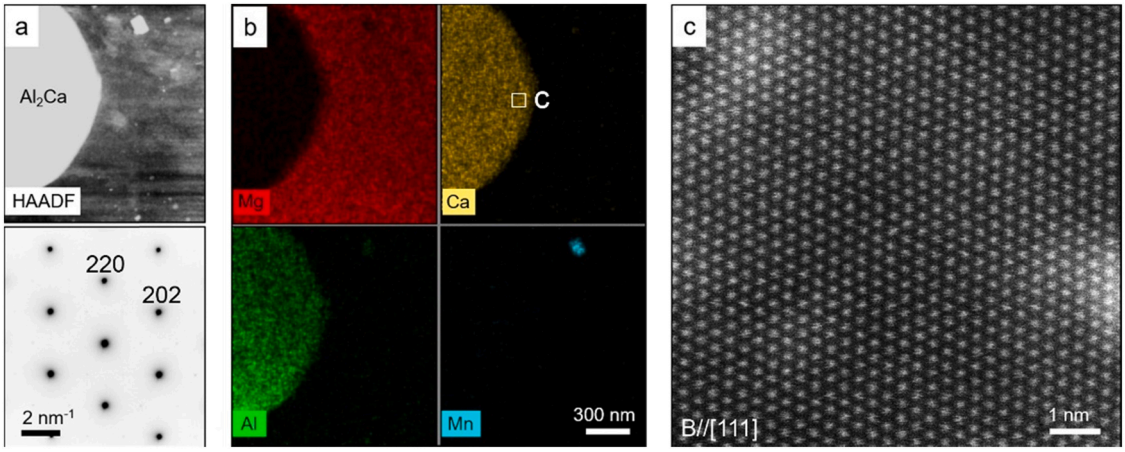

Fig. 3. Microstructure of the rolled Mg-3Al-1Ca-1Mn alloy with the C15 Laves phase observed in $[111]_{C15}$ zone axis. (a) HAADF STEM overview image and corresponding SADP of the C15 Laves phase in [111] zone axis, (b) EDS maps corresponding to the sample area shown in the HAADF image (a), (c) atomic column resolved HAADF STEM image of the C15 Laves phase corresponding to the sample area marked in (b, Ca map).

the elongation due to the formation of Al_8Mn_5 phase, as shown in Fig. S1c. Furthermore, an analysis of a normalised parameter of strain hardening capacity (Hc = (UTS-YS)/YS) in the tensile deformation (Fig. 1d, e) shows that with increasing Ca concentrations in Mg-Ca binary alloys, the strain hardening capacity decreases. With increasing Ca/Al ratio in Mg-3Al-Ca ternary alloys, the strain hardening capacity increases. A comparison of the strain hardening capacity of different deformed Mg-Al-Ca based alloys (Fig. 1f) shows that the rolled Mg-3Al-1Ca has a highest strain hardening capacity. Mg-3Al-1Ca alloy was therefore chosen for further TEM and APT characterisation.

3.2. TEM characterisation of the Ca-rich Laves phases in as-cast condition and after rolling

The Mg-3Al-1Ca alloy in the as-cast condition only contains the C36 Laves phase, which was observed by SEM-EBSD (Fig. S2) and by TEM (Fig. 2a). Selected area diffraction pattern (SADP) studies in the TEM reveal that the C36 Laves phase and the Mg matrix possess an orientation relationship (i.e. $[11\bar{2}0]_{Mg}//[11\bar{2}0]_{C36}$, $(0001)_{Mg}//(0001)_{C36}$) (Fig. 2b). HAADF-STEM and bright field TEM studies (Fig. S3) confirm the this orientation relationship and reveal a coherent $(0001)_{Mg}//(0001)_{C36}$ interface. Furthermore, two long planar stacking faults within the C36 Laves phase (with a dark contrast in (Fig. S3a)) are observed parallel to the basal plane (Fig. S3a, b). Interestingly, some fine particles with a dark contrast were observed within the C36 Laves phase under Z-contrast STEM imaging conditions (Fig. 2c). The dark contrast in STEM-HAADF indicates that the particles are most likely Mg-rich. This was confirmed by STEM-EDS analysis (Fig. 2d-j) and APT measurements (Fig. 3).

Fig. 2c provides an overview on the HAADF-STEM and STEM-EDS analysis with elemental maps for Mg, Al, Ca and the quantitative EDS analyses of the selected phases. This includes the composition of the C36 Laves phase (Fig. 2g), Mg-rich particle (Fig. 2h), the C36 Laves phase together with Mg-rich particle (Fig. 2i), and the pure Mg matrix (Fig. 2j), as marked in Fig. 2d. The thickness of the TEM foil which was used for a standardless-quantitative EDS analysis is about 30 nm as determined by low loss electron energy loss spectroscopy (EELS). The quantification of the EDS data reveals a (Mg,Al):Ca ratio of about 3:1, which is much higher than the nominal ratio of 2:1 in the form of $(Mg,Al)_2Ca$, indicating that more Mg and Al are enriched within the C36 Laves phase due to the non-equilibrium solidification condition. In addition, the composition of Al (18.3 at%) and Ca (4.5 at %) within the Mg-rich particle (Fig. 2h) is also much higher than that (Al=1.6 at% and Ca < 0.1 at%) within the Mg matrix (Fig. 2j). This may be caused by the surrounding C36 Laves phase contributing to the EDS signal.

In contrast to the C36 Laves phase in the as-cast condition (Fig. 2), after rolling, C15 Laves phase was observed in the rolled Mg-3Al-1Ca-1Mn alloy, as shown in Fig. 3a. The proof of the C15 Laves phase was based on the corresponding SADP and EDS distribution maps (Fig. 3b) as well as atomic column resolved HAADF image (Fig. 3c). It should be noted that the brighter areas observed on the HAADF image (Fig. 3c) are caused by Pt contamination at the FIB lamella surface, confirmed to originate from the unfavourable FIB preparation and not influencing the inherent material structure. All images presented in Fig. 3 were acquired with the same crystallographic orientation of the sample, corresponding to the beam direction along the [111] crystallographic direction of the cubic C15 Laves phase. SEM-EBSD scans confirm that all detected Laves phase particles belong to the C15 structure (see e.g. Fig. S4), but it cannot rule out the possibility that C36 Laves phase may be still present after rolling. At the same time, a nm-sized Mn-rich and Al-rich precipitate exists in the material, as can be observed from the EDS distribution maps (see Fig. 3b (Mn map) and further analysis in Fig S5). With the aid of SADP, atomic resolved STEM imaging and STEM-EDS mapping, the Mn-rich particles were identified as Al_8Mn_5 phase (Fig. S5).

3.3. APT characterisation of the Ca-rich Laves phases in as-cast condition and after rolling

As described in Fig. 2, Mg-rich particles were observed within C36 Laves phase in the as-cast condition. In order to further determine the distribution of Mg within C36 Laves phase in the as-cast condition, APT was used. Fig. 4 shows a 3D reconstruction of an APT measurement for the Mg-3Al-1Ca alloy containing a C36 Laves phase (Al,Ca-rich) and the Mg matrix (Mg-rich). Clearly, in the C36 Laves phase, Mg-rich particles (with sizes varying between 5 nm and several tens of nm in diameter) and two stacking faults enriched in Mg (Fig. 4f, g), exhibiting almost 2-dimensional shape (of thickness below 5 nm and length of several tens of nm), were observed. Interestingly, the APT bulk composition analysis (Table S1) reveals that the Mg-rich particles in the C36 Laves phase are with 97.3 at% Mg in agreement to the matrix (98.2 at%, Table S1). As mentioned before, the lower Mg concentration of the Mg-rich particle measured by TEM-EDS (77.2 at%, Fig. 2h) can be caused by C36 composition contributions from parts of the TEM foil. On the basis of APT observation, it can be concluded that the Mg-rich particles within the C36 Laves phase is compositionally the same as the α-Mg matrix. This

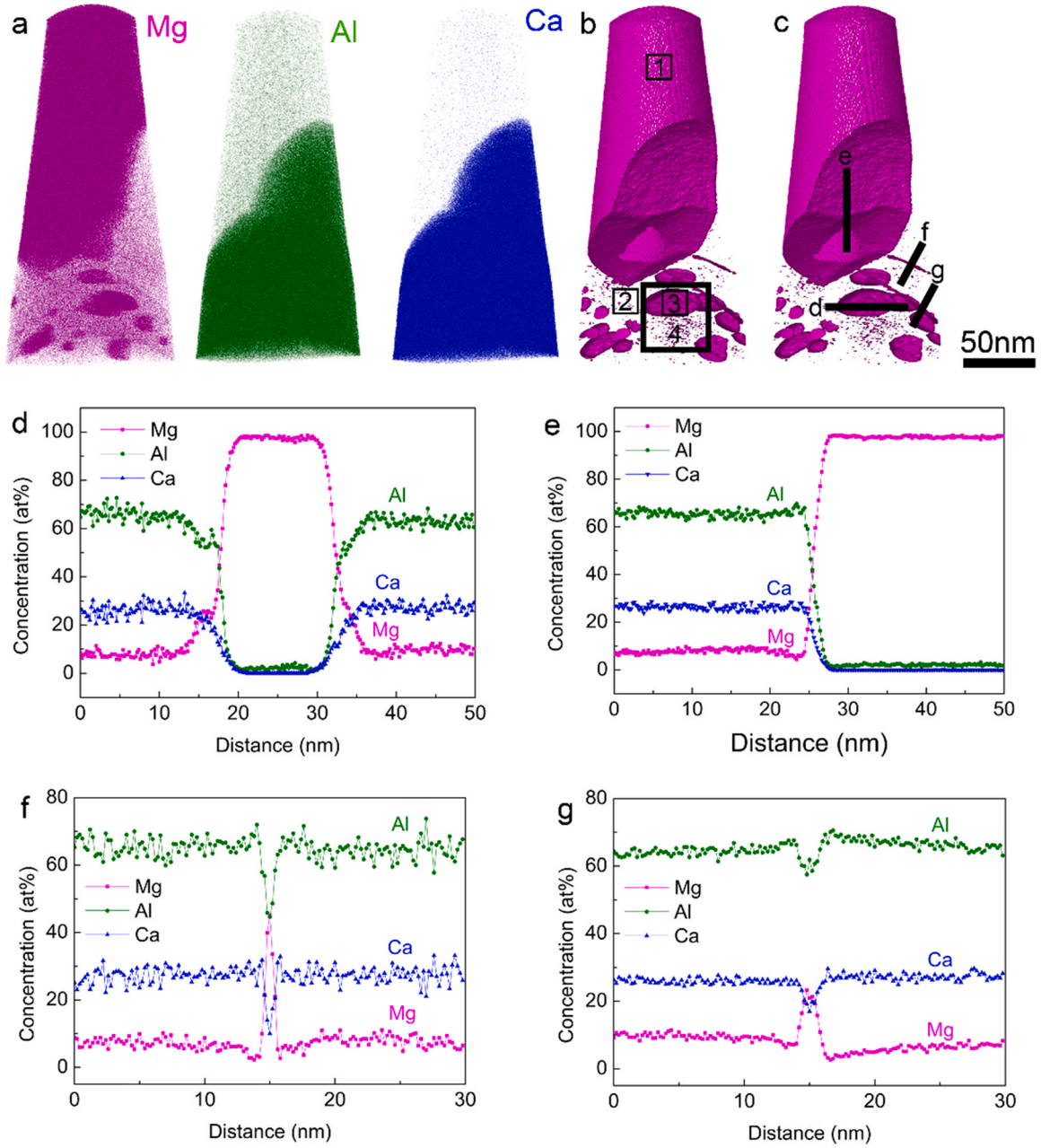

Fig. 4. 3D reconstruction of APT measurement for the Mg-3Al-1Ca alloy in the as-cast condition within the material volume containing C36 Laves phase (Al,Ca-rich) and primary α-Mg matrix (Mg-rich). (a) distribution maps of Mg, Al, and Ca. (b, c) 0.1 at% Mg isosurface. In (b), the measured regions for bulk composition were marked using 1–4. The measured bulk composition is listed in Table S1. In (c), the regions for 1D concentration profiles were marked using d-g. (d-g) 1D concentration profiles measured by a cylinder of 2 nm in diameter across the marked regions (d-g) in (c), respectively.

can be attributed to a divorced eutectic reaction under non-equilibrium solidification condition and can be regarded as eutectic Mg, as discussed later. Mg-rich clusters were also observed within the C36 Laves phase in Mg-5Al-3Ca-0.7Sr-0.2Mn alloy [36]. It should be noted that the volume of the measured regions for bulk composition analysis cannot be clearly shown in Fig. 4b in two dimensions. One 3D movie with the marked regions is therefore enclosed as movie S1.

Supplementary material related to this article can be found online at doi:10.1016/j.jallcom.2022.167177.

After rolling at 350 °C, both C36 Laves phase and C15 Laves phase were observed in Mg-3Al-1Ca alloy using APT. Fig. 5 shows a 3D reconstruction of a material volume containing an Al- and Ca-rich particle of several tens of nm in size displaying Mg, Al and Ca within the reconstructed volume. The results reveal a Ca-rich Laves phase with a layered structure (Fig. 5b). The composition profile (Fig. 5c, position marked in Fig. 5b, Ca map) through the particle confirms the presence of Al, Ca and Mg, indicating that it is likely the C36 Laves phase. Mg-rich interlayers (about 5 nm in thickness) are observed within the C36 Laves phase, which may be related to the Mg-rich particles in the as-cast condition. The concentration modulations also suggest that the transformation from the C36 Laves phase to the C15 Laves phase is not fully completed and some few C36 Laves phase still survives even after at 500 °C for 20 h and rolling at 350 °C. A trace amount of Al partitions into the C36 Laves phase, as shown in Fig. 5c.

Fig. 6a shows a 3D reconstruction of the APT measurement for the rolled Mg-3Al-1Ca alloy within the material volume only containing C15 Laves phase. The measured bulk composition is listed in Table S2. It should be noted that the volume of the measured regions for bulk composition analysis cannot be clearly shown in the two-

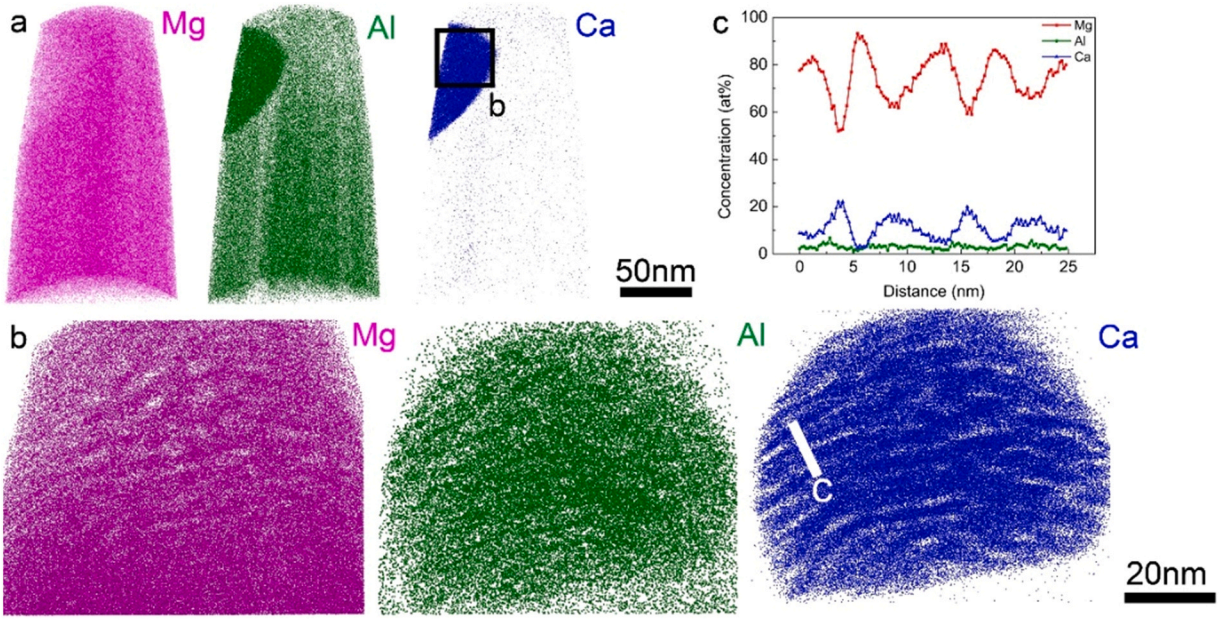

Fig. 5. 3D reconstruction of APT measurement for the rolled Mg-3Al-1Ca alloy within the material volume containing C36 Laves phase. (a) distribution maps of Mg, Al, and Ca. (b) an enlarged Mg, Al and Ca atoms map taken from the regions as marked in (a), (c) 1D concentration profile measured by a cylinder of 2 nm in diameter across the particle marked with a white line in the Ca distribution map in (b).

dimensional projection of Fig. 6b. One 3D movie with the marked regions is therefore enclosed as movie S2. The quantitative analysis (Table S2, Fig. 6c, d) confirms an overall particle composition of about 65.6 at% Al and 30.9 at% Ca, corresponding very well to the nominal composition of the C15 Laves phase (Al_2Ca). Furthermore, trace Mg (about 3.5 at%) was measured within the C15 Laves phase. Several Mg segregation layers are found locally within the C15 Laves phase (see 8 at% Mg iso-surfaces in Fig. 6b). The distribution of Al and Ca across the particle volume (Fig. 6b) is far more uniform than in the case of the C36 Laves phase in the as-cast condition (Fig. 4), strongly indicating that a significant solute distribution takes place during homogenisation and rolling. For example, Mg diffuses out of the Ca-rich Laves phase, while Al diffuses into the Ca-rich Laves phase.

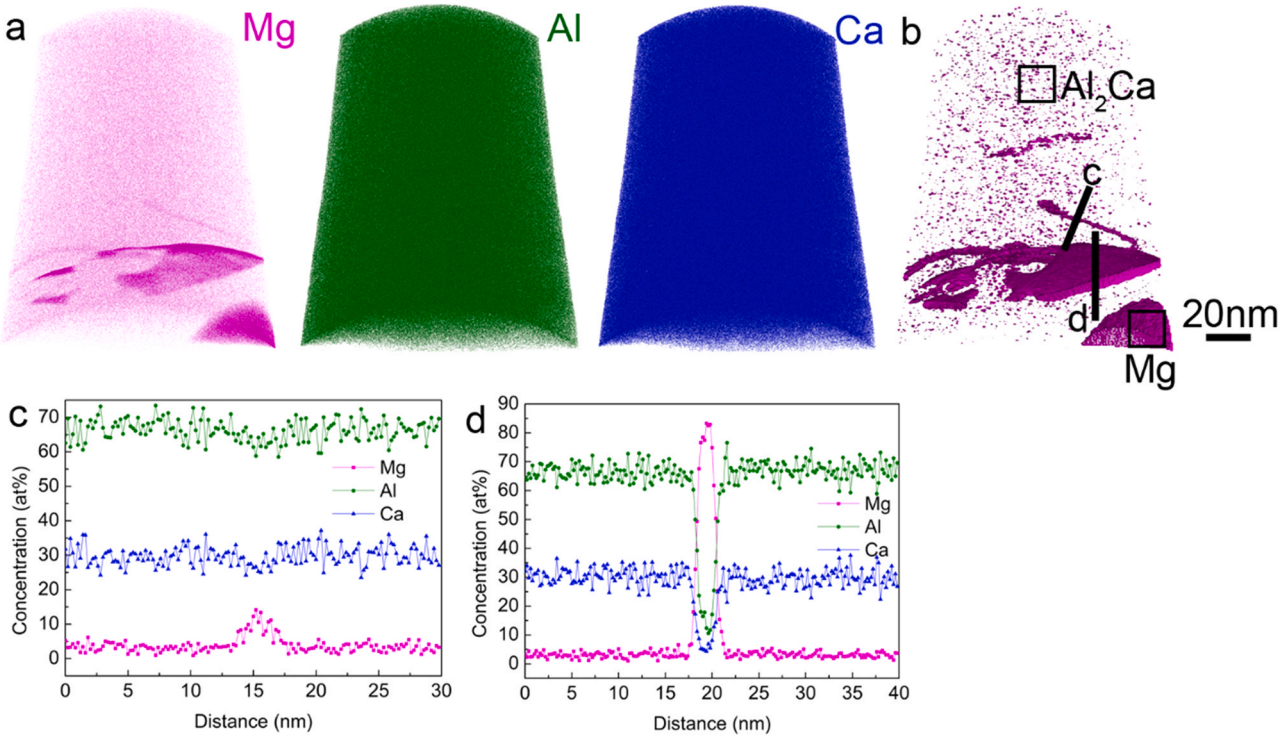

Fig. 6. 3D reconstruction of an APT measurement for the rolled Mg-3Al-1Ca alloy within the material volume only containing C15 Laves phase. (a) distribution maps of Mg, Al, and Ca. (b) the Mg isosurface using 8 at%. In (b), the measured regions for bulk composition were marked. The measured bulk composition was listed in Table S2. In (b), the measured regions for 1D concentration profile were marked using c, d. (c, d) 1D concentration profile measured by a cylinder of 2 nm in diameter across the two Mg-rich layers marked in (b).

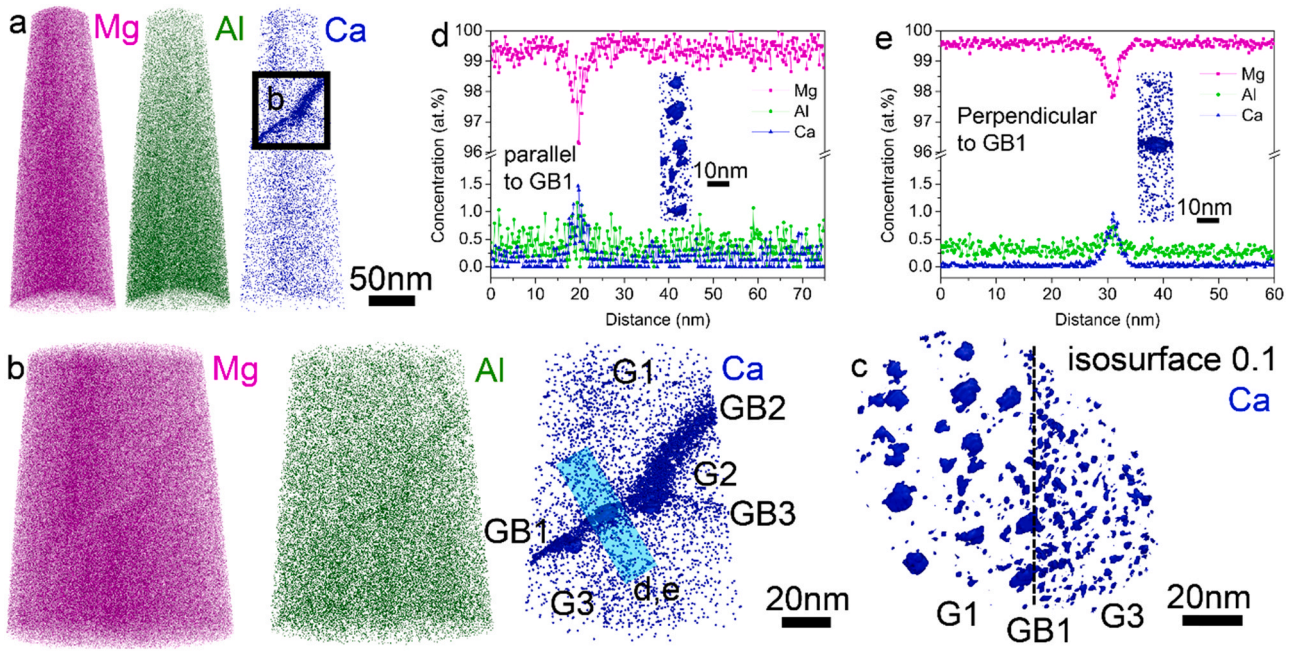

Fig. 7. 3D reconstruction of an APT measurement for the rolled Mg-3Al-1Ca alloy within the material volume containing three grain boundaries with Ca-rich clusters. (a) distribution maps of Mg, Al, and Ca. (b) an enlarged Mg, Al, and Ca map from the marked area in (a) to show three grain boundaries GB1, GB2 and GB3 separating grains G1, G2 and G3. (c) iso-surface of 0.1 at% Ca. (d, e) the composition profile extracted from a cylinder (displayed in the Ca distribution map (b)) through the particle along the GB1 (perpendicular or parallel to GB1).

Supplementary material related to this article can be found online at doi:10.1016/j.jallcom.2022.167177.

Apart from the C36 Laves phase (Fig. 5) and C15 Laves phase (Fig. 6), Fig. 7a shows a 3D reconstruction of the material volume containing three grain boundaries and Ca-rich clusters. The corresponding grains are defined as G1, G2, G3 and the grains boundaries between G1 and G3, G1 and G2, G2 and G3 are defined as GB1, GB2 and GB3, respectively. Ca-rich clusters were observed along all three grain boundaries (GB1, GB2 and GB3). However, larger Ca-rich clusters were observed along one specific grain boundary (i.e. GB1 between G1 and G3), as shown in Fig. 7c. The composition profile shown in Fig. 7d, e was extracted from a cylinder (displayed in the Ca distribution map (Fig. 7b)) through the particle along the GB1 (perpendicular or parallel to GB1) and confirms presence of Ca-rich clusters. For clarity, one movie is also enclosed as supplementary information (movie S3) to clearly show the Ca-rich clusters along these three grain boundaries. Minimum misorientation angles between the three considered grains (G1, G2 and G3) were calculated by the method described in [37] and amount to about 8.7° (G1 and G2), 17.9° (G1 and G3) and 10.7° (G2 and G3), respectively. It is worth noting that most Ca-rich particles form along GB1 with the highest misorientation angle (17.9° between G1 and G3), indicating a favourable segregation of Ca to grain boundaries with higher misorientation angles, providing higher free volume for segregation and subsequent precipitation. However, it should be noted here that besides the misorientation angles, other possible factors (i.e. the diffusion behaviour along the grain boundaries) may also need to be taken into consideration. For example, the so-called pipe diffusion [2] may occur. The solute of Al and Ca may diffuse through one grain boundary (as a diffusion channel) and then enrich into another grain boundary. The crystallographic character of the grain boundaries may also have a significant effect on the solute segregation to grain boundaries. In this sense, engineering grain boundaries can be used to tailor the solute segregation along grain boundaries. For example, increasing the density of grain boundaries with a higher misorientation angle may enhance the solute segregation along grain boundaries and thereby promote the formation of Ca-rich Laves phase. A similar Ca segregation along grain boundaries was also observed in Mg-3Al-1Zn-0.3Ca alloy [38]. However, it should be noted that in the present investigation, the Ca concentration is relatively high (about 1 wt%) compared with 0.3 wt% Ca in [38] and therefore most Ca is expected to form the Ca-rich Laves phase. No significant Ca segregation along grain boundaries was observed, which is in contrast to Al. The segregation of Al along grain boundaries was always observed in rolled Mg-3Al-1Ca alloy.

Supplementary material related to this article can be found online at doi:10.1016/j.jallcom.2022.167177.

APT analyses performed for the rolled Mg-3Al-1Ca-1Mn alloy will be discussed based on a 3D reconstruction containing two nanometre-sized Mn-rich particles and two grain boundaries in the analysed volume (Fig. 8). For clarity, one movie (movie S4) clearly shows these two nanometre-sized Mn-rich particles and two grain boundaries. A trace Ca segregation was observed in the interface between the Mn-rich particle and Mg matrix (Fig. 8b). It should be noted here that determining Ca concentration is impossible for this dataset due to its trace level. For clarity, another dataset (Fig. S6) clearly shows the Ca segregation in the interface between the Mn-rich particle and Mg matrix. 1D concentration profile extracted from a cylinder across the Mn-rich particle (Fig. 8c, as indicated in the Mn distribution map by the black cylinder of 2 nm in diameter (Fig. 8a)) reveal an Al/Mn ratio corresponding to the Al_8Mn_5 phase. This is consistent with our thermodynamic calculations (Figs. S7–9) and TEM observations (Fig. S5). Compositional analysis of one grain boundary by the concentration profile (Fig. 8d) reveals Al grain boundary segregation, while no Ca segregation was observed. This result for the rolled Mg-3Al-1Ca-1Mn alloy is in contrast to the Mn-free Mg-3Al-1Ca alloy (Fig. 7). Based on these results we speculate that the presence of Al_8Mn_5 phase can enhance the Ca enrichment at the interface of Al_8Mn_5 particles (Fig. 8b, S6, Ca map) and finally lead to the formation of the Ca-rich Laves phase.

Supplementary material related to this article can be found online at doi:10.1016/j.jallcom.2022.167177.

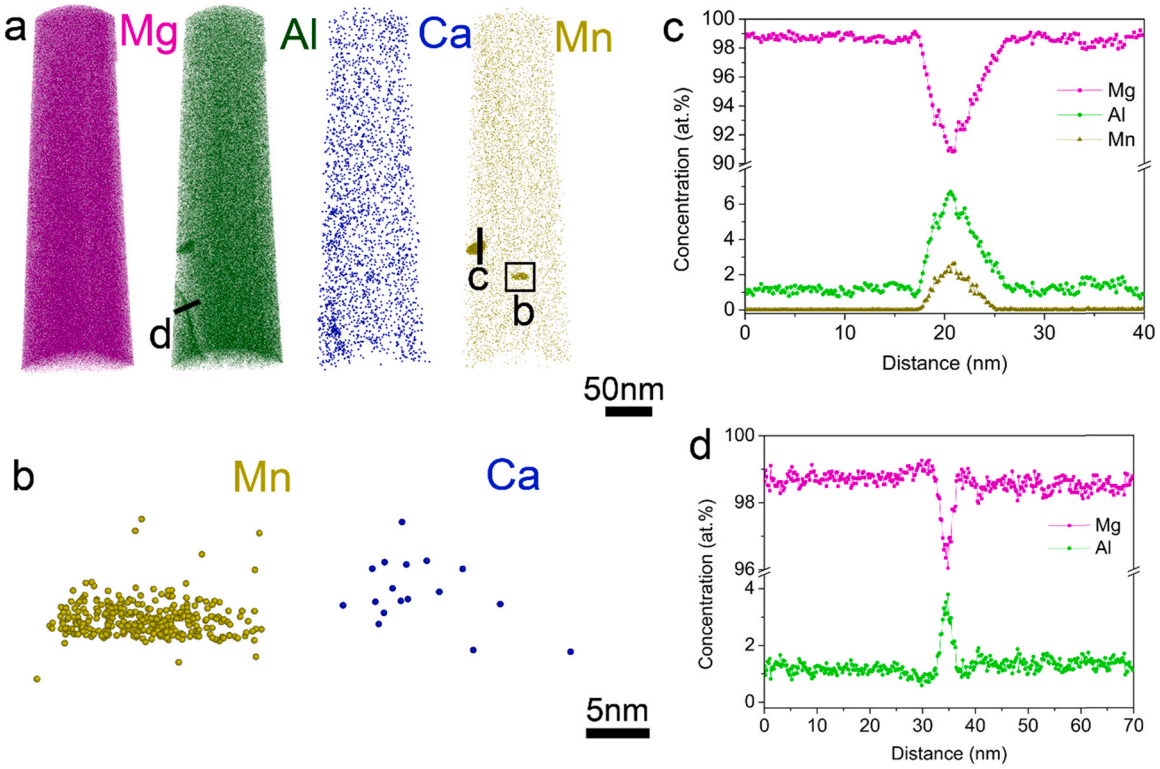

Fig. 8. 3D reconstruction of APT measurement for the rolled Mg-3Al-1Ca-Mn alloy within the material volume containing two nano-sized Al_8Mn_5 particles. (a) distribution maps of Mg, Al, Ca, and Mn. (b) an enlarged Ca and Mn map from the marked area in (a) to show the Al_8Mn_5 phase and a trace Ca segregation in the interface between Al_8Mn_5 phase and Mg matrix. (c) 1D concentration profile measured by a cylinder of 2 nm in diameter (c) across the Al_8Mn_5 phase (marked in Mn map in a) and (d) one grain boundary (marked in the Al distribution map in a).

3.4. DFT calculation on the preference of Ca-rich Laves phases

Two Ca-rich laves phases (C36 and C15) were observed using TEM (Figs. 2 and 3) and APT (Figs. 4–6). Furthermore, stacking faults were also observed within these two Ca-rich Laves phases. In order to determine the preference of Ca-rich Laves phases and the role of stacking sequence on the formation of Ca-rich Laves phase, DFT calculations was performed. The DFT calculations (Fig. 9) reveal that the energetically favourable configuration for Al-free case is the C14 Laves phase (black in Fig. 9b), whereas for Mg-free case it is the C15 Laves phase (red in Fig. 9b). This prediction is expected as the most stable phase of Mg_2Ca ($AlCa_2$) is a prototype of the C14 (C15) structure. However, it is interesting to note that, for the intermediate composition range (i.e. Al/(Al + Mg)) ratio between 0.25 and 0.75), the C36 Laves phase becomes energetically very close to both C14 Laves phase and C15 Laves phase (C15 is preferred over C14 for Al/(Al + Mg) =∼ 0.35). Considering the structural details depicted in Fig. 9a, the C14, C15 and C36 Laves phases consist of the same type of close-packed planes with different stacking sequences, which can be described by a stacking sequence of close-packed planes (shown in Fig. 9a) as AA'AA'AA' (for C14), ABCABC (for C15) and ABB'A'AB (for C36). In particular, the stacking sequence of the Ca double-planes (large green atoms) changes from AA'AA' in the C14 Laves phase, via ABCA in the C15 Laves phase to AA'BB' in the C36 Laves phase. The corresponding stacking fault energies resulting from interexchange of the stacking sequences between the three Ca-rich Laves phases, are expected to be negligibly small. This prediction of the small stacking fault energies is further strengthened by very similar specific volumes for Ca-rich Laves phases containing both Al and Mg, in particular for the C14 and C15 Laves phases, as shown in Fig. 9c. Consequently, any excess volume or incoherency stresses that can be introduced by stacking faults are expected to be reasonably low. In another case, the phase transformations and the appearance of stacking fault would be energetically strongly unfavoured.

3.5. DFT calculation on Ca segregation to the interface between Al_8Mn_5 and Mg

As shown in Fig. 8b and Fig. S5, the Ca segregation to the interface between Al_8Mn_5 and Mg was observed using APT. In order to elucidate this phenomenon, we used DFT calculations to establish a preferred substitutional site occupation for Ca in Al_8Mn_5. The energy of formation for substitution of Mn and Al sites by Ca was evaluated as a function of the local compound stoichiometry/alloy composition of the substituted site given in a form ofAl/(Al + Mn) ratio. Our results are shown in Fig. 10a and indicate that: (i) Ca preferably substitutes for Al than Mn sites, and (ii) Al-rich local neighbourhoods of the substituted Ca are slightly preferred. Subsequently, the interface structure needs to be established. To do so, a $4 \times 4 \times 3$ supercell of Mg and $1 \times 1 \times 2$ supercell of Al_8Mn_5 were joined together along the (0001) plane to form a simulation box with overall 264 atoms, as shown in Fig. 10b. It should be noted that the two structures exhibit only a small lattice mismatch (∼1.9 %) along this interface. Inspecting the structural projection presented in Fig. 10b, it can be seen that there are many possible non-equivalent shifts of the atoms of Al_8Mn_5 inside its unit cell, both in-plane and out-of-plane (with respect to the interface plane). Therefore, a series of Al_8Mn_5 unit cells, mutually differing by a uniform displacement of the atoms with respect to the unit cell reference box (i.e. each obtained by shifting all atoms in the unit cell by the same constant vector) were combined with the same $4 \times 4 \times 3$ Mg supercell. In this way, a series of 48 different interfacial structures were generated, which were subsequently structurally relaxed. The interface energy was found to reach minimum as the number of bonds across the interface is minimised (Fig. 10c); these energy convenient configurations with a

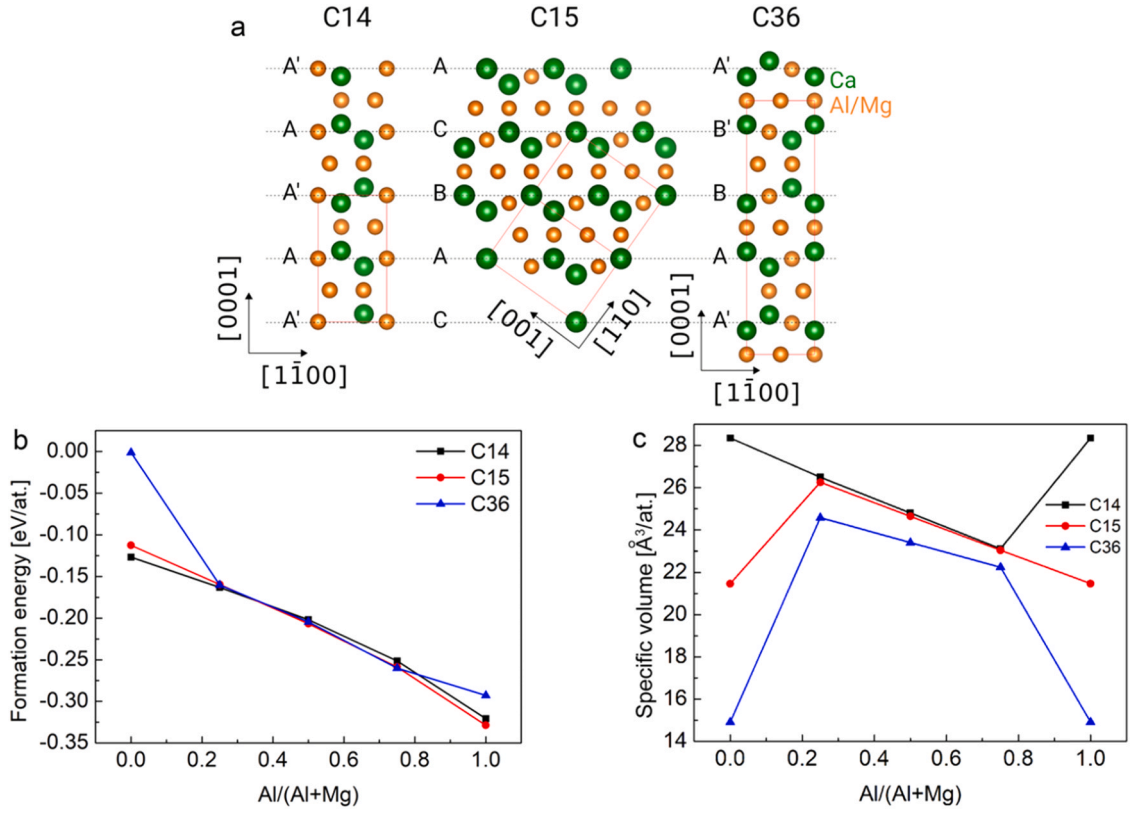

Fig. 9. DFT calculation on the preference of Ca-rich Laves phases. (a) Atom configurations of the three considered Ca-rich Laves phases (C14, C15 and C36). Formation energies (b) and specific volume (c) for the three considered Ca-rich Laves phases as a function of the alloy composition given in a form ofAl/(Al + Mg) ratio.

minimum energy contain mainly Mn-Mg bonds across the interface, whereas the number of Al-Mg bonds is minimised. The bonds were identified purely on a geometrical analysis in which nearest neighbours within a sphere of a given radius based on the respective atomic radii (2.75 Å and 2.90 Å for the Al-Mg and Mn-Mg bonds) were counted for the atoms located at the interface.

The interface with the lowest energy was chosen for further investigations; all interface atoms were one-by-one replaced by Ca, thus probing 69 interface segregation sites for Ca. Based on the change of the overall system formation energy (calculated with respect to individual species in their standard structures, Eq. (1) in the Methods), it appears that Ca strongly prefers to replace Mn in the interface, as shown in Fig. 10d. The least preferred substitution is for Mg. Thus, the interface is predicted to become Mn-lean due to the segregation (and substitution) of Ca. This indicates that the formation of Al_8Mn_5 phase may promote the Ca segregation at the interface between Al_8Mn_5 phase and Mg matrix. In this sense, optimising Mn concentration and/or Ca/Mn ratio can be used to control the formation of Ca-rich Laves phase.

4. Discussion

4.1. Formation of Mg-rich particles within C36 Laves phase via divorced eutectic reaction

Mg-rich particles within C36 Laves phase were observed using TEM (Fig. 2) and APT (Fig. 4). It should be noted here that the same structural feature was also observed in Mg-5Al-3Ca-0.7Sr-0.2Mn alloy [36], which was defined as Mg-rich clusters (with C36 structure type) within C36 Laves phase. It was assumed [36] that after the first stage of solidification of the C36 phase the liquid is depleted in Ca and Al, and therefore Mg-rich clusters can form within the eutectic. Because the contents of Ca and Al are still high, the C36 phase can still form within the eutectic C36 phase. This was attributed to the possibility of solidification of the C36 phase in a wide range of homogeneity. However, other possible formation mechanisms of Mg-rich particles still remain to be explored. One possible formation mechanism is discussed here. Mg-rich particles may form via a divorced eutectic reaction together with C36 Laves phase. It is well-known that, in the case of divorced eutectics, the two phases of the eutectic grow independently from one another. When the divorced eutectic reaction takes place at the last stage of solidification, the fraction of remaining liquid is so small that the width is comparable to the eutectic spacing. According to the Thermo-Clalc simulation (Fig. S7, S8), when the divorced eutectic reaction takes place at 540 °C, the remaining liquid is only 0.15 mol %. Furthermore, within this small highly (Al, Ca)-enriched liquid, the content of Al and Ca increases rapidly in the vicinity of the boundary. In such a situation, the eutectic phases (eutectic Mg and eutectic C36 Laves phase) may form as a layer between the primary α-Mg dendrites or just as a single particle, which fits exactly the present observation (eutectic Mg and eutectic C36 Laves phase grow together as a single particle). The coherent orientation relationship between the Mg-rich particles and the C36 Laves phase (Fig. 2b, S2) also indicates their formation by a divorced eutectic reaction. In this sense, the Mg-rich particles can be regarded as eutectic Mg. It should be noted that the presence of defects (i.e. stacking faults (Figs. S2, 4)) may promote the segregation of Mg along these defects and thereby motivate the occurrence of divorced eutectic reaction. Further investigation on the relationship between defects and divorced eutectic reaction is still needed. Furthermore, the orientation relationship between α-Mg phase (primary phase) and C36 Laves phase shows a small mismatch (Fig. 2b), indicating that C36 Laves phase may nucleate from the primary α-Mg dendrites via a divorced eutectic reaction. This type of divorced eutectic reaction has been observed experimentally and predicted using phase field simulation between eutectic $Mg_{17}Al_{12}$ (β-

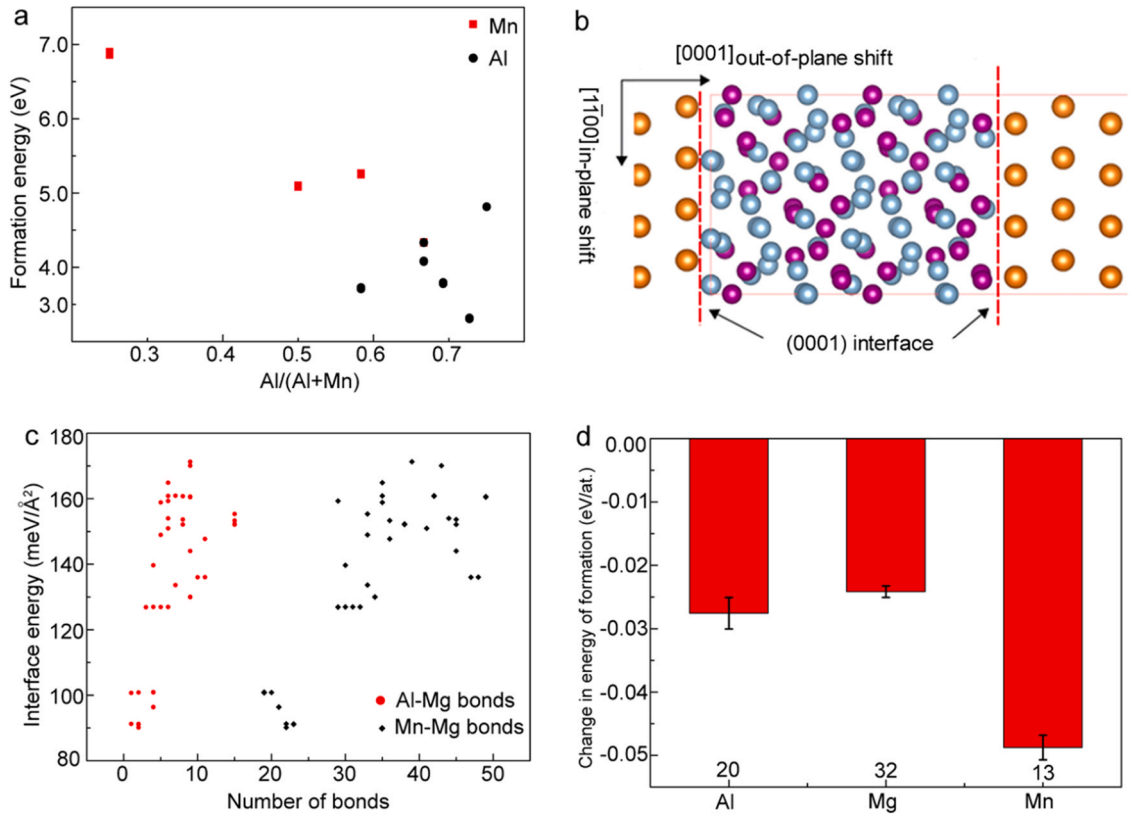

Fig. 10. (a) formation energies for substituting Al- or Mn-sites in Al_8Mn_5 by Ca, as a function of theAl/(Al + Mn) fraction. (b) schematic projection of the structure model for a 4 × 4 × 3 supercell of Mg and 1 × 1 × 2 supercell of Al_8Mn_5 with an interface parallel to the common (0001) plane (overall 264 atoms). (c) interface energy of a series of different arrangements as a function of number of bonds within the interface. (d) energy of formation changes upon Ca substitution for an interface atom for a series of different arrangements as a function of the interface site species.

phase) and eutectic Mg in Mg-Al based alloy [39,40]. However, the present observation shows that the eutectic phases (eutectic Mg and eutectic C36 Laves phase) form as a single particle.

4.2. The transformation mechanism of the Ca-rich Laves phases

Two different Ca-rich Laves phase (C36 Laves phase and C15 Laves phase) were observed using TEM and APT. These experimental observations are fully consistent with our Thermo-Calc simulations. In the as-cast condition, the C36 Laves phase forms during the solidification process via a eutectic reaction. Two types of eutectic reactions have been reported in the literature for the formation of C36 Laves phase [18]. According to our Thermo-Calc simulation (Figs. S7–9), the eutectic reaction: Liq → eutectic Mg + C36 is most likely to occur, which suggests that C36 Laves phase forms directly from the liquid, together with eutectic Mg. During the solution treatment applied in our study (500 °C for 20 h), the C36 Laves phase gradually transforms into the C15 Laves phase or the C15 Laves phase forms separately independent of the C36 Laves phase, as shown in Figs. 4–6. At least two aspects should be taken into consideration when discussing the possible transformation mechanism. The first aspect is the change of the composition within the Ca-rich Laves phases. As reported in [19], within the eutectic region, α-Mg contains excess Al due to the fact that the solubility limit of Al in α-Mg decreases with decreasing temperature. During our solution treatment, the excess Al can diffuse into C36 Laves phase and impose a change in its Mg:Al ratio and thereby induce the phase transformation from C36 Laves phase into Al-rich C15 Laves phase. DFT calculations (Fig. 9) also support this phase transformation from C36 Laves phases to C15 Laves phase due to the fact that the formation energy and specific volume of the C36 Laves phases is marginally lower than that of C15 Laves phase with increasing theAl/(Al + Mg) fraction up to 0.8. The second aspect of the possible transformation mechanism is the change of the stacking sequence. As discussed above (Fig. 9), the C15 Laves phases and C36 Laves phases consist of the same type of close-packed planes with different stacking sequences. The transformation from C36 Laves phases to C15 Laves phase was reported to be geometrically possible by a shear mechanism via synchro-Shockley dislocations [41,42]. Our DFT calculations (Fig. 9) provide evidence that the corresponding stacking fault energies are negligibly small. Accordingly, formation of the planar stacking fault within the C36 and C15 Laves phases becomes very likely to occur, which can be further supported by TEM and APT observations in Figs. S2a, b, 4 (for C36 Laves phases) and Fig. 6 (for C15 Laves phases). The combined effect of the partitioning of Al into the C36 Laves phase and the change of the stacking sequence leads to the transformation from C36 to the C15 Laves phase. This transformation sequence is also consistent with the results of Min et al. [16] who found that the bond network of the C15 Laves phase has a higher bond energy and stability than that of C36 Laves phase. Due to the presence of deformable C15 Laves phase, the mechanical properties, in particular the strain hardening capacity, improve, as shown in Fig. 1.

5. Conclusions

In summary, we have investigated the segregation of Ca into grain boundaries and formation of Ca-rich clusters or Ca-rich Laves phases in Mg-3Al-1Ca and Mg-3Al-1Ca-1Mn alloys in three processing conditions (as-cast, homogenised (500 °C, 20 h), and rolled (350 °C)). In as-cast condition, Mg-rich particles with an oval morphology, a size of 20 nm and an enrichment of trace Al (8.6 at%) were

observed within C36 Laves phase, which can be attributed to the divorced eutectic reaction under non-equilibrium solidification condition. After homogenisation at 500 °C for 20 h and/or rolling at 350 °C, the C36 Laves phase has transformed into the C15 Laves phase. The transformation mechanism from C36 to C15 Laves phase is postulated to take place in terms of the diffusion of Mg out of C36 Laves phase, the partitioning of Al into C36 Laves phase and the change of stacking sequences. The latter is further supported by the negligibly small difference in DFT calculated stacking fault energies between the three Ca-rich Laves phases. Two types of Ca segregation were observed. Firstly, APT revealed a strong Ca segregation to grain boundaries with a high misorientation angle, which is proposed to play a role as a precursor for the formation of the Ca-rich Laves phases (i.e. C36 Laves phase and/or C15 Laves phase). Secondly, Ca segregation at the interface between Al_8Mn_5 and Mg matrix was also observed via APT. Again, DFT calculations reveal that the formation of Al_8Mn_5 phase may promote the Ca segregation to the Al_8Mn_5 - Mg matrix interface, as the Mn-lean and Ca-enriched interfaces between both are found to be energetically favourable. On the basis of these two types of Ca segregations, two possible concepts (by engineering grain boundaries and tailoring the solute segregation of Al and Ca along grain boundaries, or by optimising Mn concentration and Ca/Mn ratio) were therefore proposed to further improve performance of Mg-Al-Ca-Mn based alloys.

CRediT authorship contribution statement

Jiehua Li designed the project, performed experiments, wrote the original draft and edited the submitted draft. **Xuyang Zhou, Zirong Peng, Philipp Kürnsteiner** and **Andrew Breen** performed APT experiments and data analysis. **Jing Su**: performed SEM EBSD experiments. **Maria Jazmin Duarte Correa** conducted the FIB experiments. **Marta Lipińska-Chwałek** contributed with STEM HAADF and EDS experiments and data analysis, and edited the draft. **Huiyuan Wang** performed melting, casting and rolling experiments. **David Holec** performs DFT calculation, and edited the draft. **Joachim Mayer** and **Gerhard Dehm** discussed the work and edited the manuscript. All authors contributed to the interpretation of the results and to the writing of the paper.

Data Availability

Data will be made available on request.

Declaration of Competing Interest

The authors declare that they have no known competing financial interests or personal relationships that could have appeared to influence the work reported in this paper.

Acknowledgements

J.H. Li acknowledges the host from Prof Dierk Raabe, technical support from the staffs, the APT help from Junyang He and Baptiste Gault in Max-Planck Institut für Eisenforschung and the financial support from Humboldt Research Fellowships for Experienced Researcher, Austrian Science Fund (No. P 32378-N37), BMBWF (KR 06/2020). X. Zhou is supported by the Alexander von Humboldt-Stiftung. The DFT computational results have been achieved using the Vienna Scientific Cluster (VSC). Marta Lipińska-Chwałek, Joachim Mayer and Gerhard Dehm acknowledge the financial support from the Deutsche Forschungsgemeinschaft (DFG) within the Collaborative Research Centre SFB 1394: Structural and Chemical Atomic Complexity - From Defect Phase Diagrams to Material Properties, project ID 409476157. STEM experiments were performed at the Ernst Ruska-Center (ER-C) for Microscopy and Spectroscopy with Electrons, Forschungszentrum Jülich (FZJ) in Germany. The ER-C beam-time access for J.H. Li was provided via the DFG Core Facility Project ER-C D-030 and funding from the European Union's Horizon 2020 research and innovation program under grant agreement No 823717-ESTEEM3 (ID 543).

Data Availability

The data that support the findings of this study are available from the corresponding author upon reasonable request.

Appendix A. Supporting information

Supplementary data associated with this article can be found in the online version at doi:10.1016/j.jallcom.2022.167177.

References

[1] B.L. Mordike, T. Ebert, Magnesium properties — applications — potential, Mater. Sci. Eng. A 302 (2001) 37–45, https://doi.org/10.1016/S0921-5093(00)01351-4
[2] J.F. Nie, Precipitation and hardening in magnesium alloys, Metall. Mater. Trans. A 43 (2012) 3891–3939, https://doi.org/10.1007/s11661-012-1217-2
[3] G. Zhu, L. Wang, J. Wang, J. Wang, J. Park, X. Zeng, High deformable Mg-Al-Ca alloy with Al_2Ca precipitates, Acta Mater. 200 (2020) 236–245, https://doi.org/10.1016/j.actamat.2020.09.006
[4] T. Trang, J. Zhang, J. Kim, A. Zargaran, J. Hwang, B. Suh, N. Kim, Designing a magnesium alloy with high strength and high formability, Nat. Commun. 9 (2018) 2522, https://doi.org/10.1038/s41467-018-04981-4
[5] G. Zhu, L. Wang, H. Zhou, J. Wang, Y. Shen, P. Tu, H. Zhu, W. Liu, P. Jin, X. Zeng, Improving ductility of a Mg alloy via non-basal < a > slip induced by Ca addition, Int. J. Plast. 120 (2019) 164–179, https://doi.org/10.1016/j.ijplas.2019.04.020
[6] K. Maruyama, M. Suzuki, H. Sato, Creep strength of magnesium-based alloys, Metall. Mater. Trans. A 33 (2002) 875–882, https://doi.org/10.1007/s11661-002-1020-6
[7] B.L. Mordike, Creep-resistant magnesium alloys, Mater. Sci. Eng. A 324 (2002) 103–112, https://doi.org/10.1016/S0921-5093(01)01290-4
[8] S.M. Zhu, B.L. Mordike, J.F. Nie, Creep and rupture properties of a squeeze-cast Mg-Al-Ca alloy, Metall. Mater. Trans. A 37 (2006) 1221–1229, https://doi.org/10.1007/s11661-006-1073-z
[9] S.M. Zhu, B.L. Mordike, J.F. Nie, Creep properties of a Mg–Al–Ca alloy produced by different casting technologies, Mater. Sci. Eng. A 483–484 (2008) 583–586, https://doi.org/10.1016/j.msea.2006.09.154
[10] N.D. Saddock, A. Suzuki, J.W. Jones, T.M. Pollock, Grain-scale creep processes in Mg–Al–Ca base alloys: Implications for alloy design, Scr. Mater. 63 (2010) 692–697, https://doi.org/10.1016/j.scriptamat.2010.03.055
[11] T. Homma, S. Nakawaki, S. Kamado, Improvement in creep property of a cast Mg–6Al–3Ca alloy by Mn addition, Scr. Mater. 63 (2010) 1173–1176, https://doi.org/10.1016/j.scriptamat.2010.08.033
[12] T. Homma, S. Nakawaki, K. Oh.Ishi, K. Hono, S. Kamado, Unexpected influence of Mn addition on the creep properties of a cast Mg-2Al-2Ca (mass %) alloy, Acta Mater. 59 (2011) 7662–7672, https://doi.org/10.1016/j.actamat.2011.08.049
[13] Y. Nakaura, A. Watanabe, K. Ohori, Effects of Ca,Sr additions on properties of Mg-Al based alloys, Mater. Trans. 47 (2006) 1031–1039, https://doi.org/10.2320/matertrans.47.1031
[14] A. Suzuki, N.D. Saddock, J.W. Jones, T.M. Pollock, Phase equilibria in the Mg-Al-Ca ternary system at 773 and 673 K, Metall. Mater. Trans. A 37 (2006) 975–983, https://doi.org/10.1007/s11661-006-0070-6
[15] D. Kevorkov, M. Medraj, J. Li, E. Essadiqi, P. Chartrand, The 400 °C isothermal section of the Mg-Al-Ca system, Intermetallics 18 (2010) 1498–1506, https://doi.org/10.1016/j.intermet.2010.03.038
[16] X.G. Min, Y.S. Sun, F. Xue, W.W. Du, D.Y. Wu, Analysis of valence electron structures (VES) of intermetallic compounds containing calcium in Mg-Al-based alloys, Mater. Chem. Phys. 78 (2003) 88–93, https://doi.org/10.1016/S0254-0584(02)00312-7
[17] Y. Zhong, J. Liu, R.A. Witt, Y. Sohn, Z.K. Liu, Al_2(Mg,Ca) phases in Mg–Al–Ca ternary system: first-principles prediction and experimental identification, Scr. Mater. 55 (2006) 573–576, https://doi.org/10.1016/j.scriptamat.2006.03.068
[18] H. Cao, C. Zhang, J. Zhu, G. Cao, S. Kou, R. Schmid-Fetzer, Y.A. Chang, Experiments coupled with modeling to establish the Mg-rich phase equilibria of Mg–Al–Ca, Acta Mater. 56 (2008) 5245–5254, https://doi.org/10.1016/j.actamat.2008.07.003
[19] A. Suzuki, N.D. Saddock, J.W. Jones, T.M. Pollock, Structure and transition of eutectic Mg,Al_2Ca Laves phase in a die-cast Mg-Al-Ca base alloy, Scr. Mater. 51 (2004) 1005–1010, https://doi.org/10.1016/j.scriptamat.2004.07.011
[20] J.R. TerBush, A. Suzuki, N.D. Saddock, J.W. Jones, T.M. Pollock, Dislocation substructures of three die-cast Mg–Al–Ca-based alloys, Scr. Mater. 58 (2008) 914–917, https://doi.org/10.1016/j.scriptamat.2008.01.015
[21] S.M. Liang, R.S. Chen, J.J. Blandin, M. Suery, E.H. Han, Thermal analysis and solidification pathways of Mg–Al–Ca system alloys, Mater. Sci. Eng. A 480 (2008) 365–372, https://doi.org/10.1016/j.msea.2007.07.025

[22] S.W. Xu, K. Oh-ishi, S. Kamado, F. Uchida, T. Homma, K. Hono, High-strength extruded Mg–Al–Ca–Mn alloy, Scr. Mater. 65 (2011) 269–272, https://doi.org/10.1016/j.scriptamat.2011.04.026
[23] M.Z. Bian, T.T. Sasaki, B.C. Suh, T. Nakata, S. Kamado, K. Hono, A heat-treatable Mg-Al-Ca-Mn-Zn sheet alloy with good room temperature formability, Scr. Mater. 138 (2017) 151–155, https://doi.org/10.1016/j.scriptamat.2017.05.034
[24] M. Cihova, R. Schäublin, L.B. Hauser, S.S.A. Gerstl, C. Simson, P.J. Uggowitzer, J.F. Löffler, Rational design of a lean magnesium-based alloy with high age-hardening response, Acta Mater. 158 (2018) 214–229, https://doi.org/10.1016/j.actamat.2018.07.054
[25] T. Nakata, C. Xu, R. Ajima, K. Shimizu, S. Hanaki, T.T. Sasaki, L. Ma, K. Hono, S. Kamado, Strong and ductile age-hardening Mg-Al-Ca-Mn alloy that can be extruded as fast as aluminum alloys, Acta Mater. 130 (2017) 261–270, https://doi.org/10.1016/j.actamat.2017.03.046
[26] H.C. Pan, G.W. Qin, Y.M. Huang, Y.P. Ren, X.C. Sha, X.D. Han, Z.Q. Liu, C.F. Li, X.L. Wu, H.W. Chen, C. He, L.J. Chai, Y.Z. Wang, J.F. Nie, Development of low-alloyed and rare-earth-free magnesium alloys, Acta Mater. 149 (2018) 350–363, https://doi.org/10.1016/j.actamat.2018.03.002
[27] S. Sandlöbes, M. Friák, S. Korte-Kerzel, Z. Pei, J. Neugebauer, D. Raabe, A rare-earth free magnesium alloy with improved intrinsic ductility, Sci. Rep. 7 (2017) 10458, https://doi.org/10.1038/s41598-017-10384-0
[28] G.B. Thompson, M.K. Miller, H.L. Fraser, Some aspects of atom probe specimen preparation and analysis of thin film materials, Ultramicroscopy 100 (2004) 25–34, https://doi.org/10.1016/j.ultramic.2004.01.010
[29] M. Schaffer, B. Schaffer, Q. Ramasse, Sample preparation for atomic-resolution STEM at low voltages by FIB, Ultramicroscopy 114 (2012) 62–71, https://doi.org/10.1016/j.ultramic.2012.01.005
[30] G. Kresse, J. Furthmüller, Efficiency of ab-initio total energy calculations for metals and semiconductors using a plane-wave basis set, Comput. Mater. Sci. 6 (1996) 15–50, https://doi.org/10.1016/0927-0256(96)00008-0
[31] G. Kresse, J. Furthmüller, Efficient iterative schemes for ab initio total-energy calculations using a plane-wave basis set, Phys. Rev. B Condens. Matter 54 (1996) 11169–11186, https://doi.org/10.1103/PhysRevB.54.11169
[32] G. Kresse, D. Joubert, From ultrasoft pseudopotentials to the projector augmented-wave method, Phys. Rev. B Condens. Matter 59 (1999) 1758, https://doi.org/10.1103/PhysRevB.59.1758
[33] J.P. Perdew, K. Burke, M. Ernzerhof, Generalized gradient approximation made simple, Phys. Rev. Lett. 77 (1996) 3865–3868, https://doi.org/10.1103/PhysRevLett.77.3865
[34] H.J. Monkhorst, J.D. Pack, Special points for Brillouin-zone integrations, Phys. Rev. B Condens. Matter 13 (1976) 5188, https://doi.org/10.1103/PhysRevB.13.5188
[35] K. Momma, F. Izumi, VESTA3 for three-dimensional visualization of crystal, volumetric and morphology data, J. Appl. Crystallogr 44 (2011) 1272–1276, https://doi.org/10.1107/S0021889811038970
[36] Tomasz Rzychoń, Characterization of Mg-rich clusters in the C36 phase of the Mg-5Al-3Ca-0.7Sr-0.2Mn alloy, J. Alloy. Compd. 598 (2014), https://doi.org/10.1016/j.jallcom.2014.02.029 (95-10).
[37] A.J. Breen, K. Babinsky, A.C. Day, K. Eder, C.J. Oakman, P.W. Trimby, S. Primig, J.M. Cairney, S.P. Ringer, Correlating atom probe crystallographic measurements with transmission Kikuchi diffraction data, Microsc. Microanal. 23 (2017) 279–290, https://doi.org/10.1017/S1431927616012605
[38] R. Pei, Y. Zou, D. Wei, T. Al-Samman, Grain boundary co-segregation in magnesium alloys with multiple substitutional elements, Acta Mater. 208 (2021) 116749, https://doi.org/10.1016/j.actamat.2021.116749
[39] A. Monas, O. Shchyglo, S. Kim, C.D. Yim, D. Höche, I. Steinback, Divorced eutectic solidification of Mg-Al alloys, JOM 67 (2015) 1805–1811, https://doi.org/10.1007/s11837-015-1418-4
[40] J.H. Kang, J. Park, K. Song, C.S. Oh, O. Shchyglo, I. Steinbach, Microstructure analyses and phase-field simulation of partially divorced eutectic solidification in hypoeutectic Mg-Al Alloys, J. Magnes. Alloy. 10 (2022) 1672–1679, https://doi.org/10.1016/j.jma.2021.04.014
[41] P.M. Hazzledine, P. Pirouz, Synchroshear transformations in Laves phases, Scr. Matall Mater. 28 (1993) 1277–1282, https://doi.org/10.1016/0956-716X(93)90468-8
[42] K.S. Kumar, D.B. Miracle, Polytypic transformations in Laves phases, Intermetallics 12 (2004) 763–770, https://doi.org/10.1016/j.intermet.2004.02.017